1 **Iron and manganese shuttles control the formation of authigenic phosphorus minerals in**

2 **the euxinic basins of the Baltic Sea**

3 Tom Jilbert[1*], Caroline P. Slomp[1]

4

5

6

7

8

9

10

11

12

13

14

15

16

17

18

19

20

21

22

23 [*]Corresponding author (T.S.Jilbert@uu.nl), Tel +31 30 253 5037, Fax +31 30 253 5302

24 [1] Department of Earth Sciences (Geochemistry), Faculty of Geosciences, Utrecht University,

25 P.O. Box 80.021, 3508 TA Utrecht, The Netherlands.

ABSTRACT

Microanalysis of epoxy resin-embedded sediments is used to demonstrate the presence of authigenic iron (Fe) (II) phosphates and manganese (Mn)- calcium (Ca)- carbonate-phosphates in the deep euxinic basins of the Baltic Sea. These minerals constitute major burial phases of phosphorus (P) in this area, elevating the total P burial rate above that expected for a euxinic depositional environment. Particle shuttles of Fe and Mn oxides into the deep euxinic basins act as drivers for P-bearing mineral authigenesis. While Fe (II) phosphates are formed continuously in the upper sediments following the sulfidization of Fe-oxyhydroxides and release of associated P, Mn-Ca-carbonate-phosphates are formed intermittently following inflow events of oxygenated North Sea water into the deep basins. The mechanism of Fe (II) phosphate formation differs from previously reported occurrences of vivianite formation in marine sediments, by occurring within, rather than below, the sulfate-methane transition zone. The spatial distribution of both authigenic phases in Baltic sediments varies in accordance with the periodic expansion of anoxia on centennial to millennial timescales. The results highlight the potential importance of authigenic P-bearing minerals other than carbonate fluorapatite for total P burial in euxinic basins.

1. INTRODUCTION

Phosphorus (P) is the ultimate limiting nutrient for marine biological production, due to the ability of pelagic cyanobacteria to fix nitrogen (N) from the atmosphere and thus to make up any deficit in the supply of nitrate (NO_3^-) relative to phosphate (HPO_4^{2-}) in surface waters (Tyrrell, 1999). Hence, the availability of P in marine systems controls the rate of organic matter production. Phosphorus availability, in turn, is controlled by the balance between the input of P from rivers and the atmosphere, internal recycling and exchange with adjacent marine basins, and finally removal through burial in sediments (Ruttenberg, 2003).

The flux of P to the oceans can vary naturally on geological timescales (Tsandev and Slomp, 2009), while on the shorter timescale of recent decades, anthropogenic loading of both P and N has led to the eutrophication of coastal systems worldwide (e.g. Elmgren, 2001; Turner et al., 2006). By influencing organic matter production, P also exerts a strong control on oxygen concentrations in the oceans due to the oxygen demand of organic matter respiration. Moreover, positive feedbacks within the P cycle amplify this relationship. Under low-oxygen conditions, P is preferentially remineralized (relative to carbon and nitrogen) from sedimentary organic matter. This process stimulates efficient P recycling to surface waters, fuelling further production and a high biological oxygen demand (Ingall et al., 1993; Jilbert et al., 2011). The reduction of sedimentary iron (Fe)-oxyhydroxides under low-oxygen conditions also lowers the potential of sediments to 'trap' P close to the sediment-water interface (Mortimer, 1941), further increasing the efficiency of P regeneration.

Sediment P burial represents the long-term output of the marine P cycle, and thus has the potential to break the feedback loop between P regeneration, high biological production

76 and low-oxygen conditions. Phosphorus may be buried in sediments within various distinct

77 fractions. These include organic matter, detrital phosphate minerals and authigenic mineral

78 phases (Ruttenberg, 1992). Authigenic P-bearing phases buried in sediments include P

79 associated with Fe-oxyhydroxides which resist reduction in the upper sediments (Reed et al.,

80 2011), calcium (Ca)-phosphates such as carbonate fluorapatite (e.g. Ruttenberg and Berner,

81 1993) and P associated with manganese (Mn)-Ca-carbonates (Mort et al., 2010; Suess, 1979),

82 and finally Fe (II) phosphates such as vivianite (e.g. Burns, 1997).

83

84   Carbonate fluorapatite (CFA), $Ca_{10}(PO_4)_{6-x}(CO_3)_x(OH,F)_{2+x}$, forms either by direct

85 nucleation from saturated porewaters (Van Cappellen and Berner, 1989), via precursor phases

86 (Gunnars et al., 2004; Jahnke et al., 1983) or by conversion of calcite microfossils within the

87 sediments (Manheim et al., 1975). CFA formation has been shown to occur in a range of

88 coastal and deep-sea environments worldwide (Filippelli and Delaney 1996; Ruttenberg and

89 Berner 1993; Slomp et al., 1996) and is considered the most important authigenic sink for P in

90 the marine realm, accounting for an estimated 50% of global P burial (Ruttenberg, 1993).

91

92   In contrast to Ca-phosphates, the formation of vivianite, $Fe_3(PO_4)_2 \cdot 8(H_2O)$, in marine

93 sediments has been reported only in a few locations (Burns, 1997; März et al., 2008;

94 Ruttenberg and Goni, 1997; Schulz et al., 1994). Mostly, vivianite formation has been

95 observed in environments where porewaters are rich in dissolved Fe, implying supersaturation

96 with respect to vivianite. Porewater Fe accumulation is most likely to occur below the sulfate-

97 methane transition zone (SMT) of marine sediments, where sulfide production is absent. In

98 the presence of hydrogen sulfide, dissolved Fe is expected to be rapidly sequestered into the

99 solid phase, maintaining undersaturation of the porewaters with respect to vivianite.

100

101   Despite the established knowledge of enhanced P regeneration from organic matter

102   under low-oxygen conditions (Ingall et al., 1993), the processes controlling sequestration of P

103   into authigenic minerals in low-oxygen environments are poorly constrained. Improved

104   knowledge of these processes is required to better constrain the global rate of P burial in

105   marine sediments, and consequently the relationships with the global carbon and oxygen

106   cycles (Van Cappellen and Ingall, 1996). The modern expansion of low-oxygen conditions in

107   the coastal zone (Diaz and Rosenberg, 2008) and the open ocean (Stramma et al., 2008) adds

108   a particular urgency to this need. Recent work has suggested that sedimentary bacteria may

109   influence Ca-phosphate authigenesis in some low-oxygen coastal environments (Goldhammer

110   et al., 2010; Schulz and Schulz 2005), but the global importance of this process is still

111   unknown. Moreover, both the mechanisms and global importance of Fe (II) phosphate

112   precipitation in low-oxygen sediments remain to be established.

113

114   Here we present data from one of the world's largest anoxic water bodies, the Baltic

115   Sea, which suggest that Fe (II) phosphates play an important role in sediment P burial in

116   euxinic basins. We present direct evidence for currently-forming sedimentary Fe-phosphate

117   minerals, obtained from microanalysis of epoxy resin-embedded sediments. Using porewater

118   chemical data we show how the formation mechanism of Fe (II) phosphates differs from those

119   reported in earlier studies, suggesting that Fe (II) phosphate authigenesis may be more widely

120   distributed in low-oxygen marine sediments than previously thought. We also confirm the

121   importance of Mn-Ca-carbonates as a sink for P in Baltic sediments and demonstrate the role

122   of specific microfossils in sequestering P as apatite. Finally, by analyzing sediment cores

123   capturing the past ~8000 years, we show how authigenesis of P-bearing minerals has varied in

124   the Baltic throughout the Holocene.

125

2. STUDY SITES AND CORE COLLECTION

126

127

128   Sediment cores were recovered using a multi-corer and gravity corer from three sites

129 in the central Baltic Sea during multiple sampling campaigns (Fig. 1). Details of the sites and

130 the data collected during each sampling campaign are given in Table 1. This study focuses

131 principally on two sites (F80 and LL19) located within the deep central basins of the Baltic.

132 One shallower site (LF1) is studied as a reference for processes occurring on the margins of

133 the deep basins.

134

135   The sediments at all sites have accumulated during the current brackish phase of the

136 Holocene history of the Baltic, referred to as the Littorina Sea stage (e.g. Winterhalter et al.,

137 1981). The Littorina was initiated between 9000 and 7000 yr BP, and its sediments are

138 characterized by elevated organic carbon contents (Sohlenius et al., 2001). Three distinct

139 phases of enhanced Baltic-wide anoxia have been identified in the Littorina sedimentary

140 record, corresponding to the Early Holocene (~8000 yr BP to 4000 yr BP), the Medieval

141 Climate Anomaly (MCA, ~1100 yr BP to 650 yr BP) and the modern anoxic interval from the

142 late 20th century to present (Zillen et al., 2008).

143

144   The expansion of modern anoxia in the Baltic is principally driven by anthropogenic

145 nutrient loading (Conley et al., 2009). Bottom waters in the deep basins today are frequently

146 euxinic, with hydrogen sulfide concentrations rising to > 20 μmol/L between major inflow

147 events of more saline and oxygenated North Sea water (Baltic Environmental Database,

148 http://nest.su.se/models/bed.htm). Both deep basin sites (F80 and LL19) were subject to an

149 inflow in 2003 but were euxinic at the time of sampling. Hence, by the scheme of Mort et al.

150 (2010) and Jilbert et al. (2011), these sites classify as 'Group 2' (permanently hypoxic/anoxic)

151   while the shallow reference site LF1 classifies as 'Group 1' (oxic/seasonally hypoxic, Table

152   1).

153

154

155   **3. ANALYTICAL METHODS**

156

157   3.1 Epoxy embedding and microanalysis

158   Mini sub-cores from sediment multicores were embedded, vertically intact, with epoxy

159   resin in preparation for elemental microanalysis. Sediment was pushed upwards from the

160   multicore tubes into a series of shorter (7 cm-length) tubes of equivalent diameter, which were

161   separated by inserting horizontal dividers. Mini sub-cores were then taken from the 7 cm-

162   length multicore sections using cutoff 1 cm-diameter centrifuge tubes. The cutoff centrifuge

163   tubes were inverted, inserted into the sediment and capped at the base with a hollow cap, after

164   insertion of a piece of filter cloth between cap and tube. The mini sub-cores were then

165   transferred to acetone baths in a polyethylene argon-filled glovebox and subsequently

166   embedded with Spurr's epoxy resin (Jilbert et al., 2008, note that no desalination step was

167   performed in the present study). Horizontally-oriented samples from gravity core sections

168   were also embedded after extraction from the open core surface with aluminium trays.

169

170   After curing, epoxy-embedded samples were opened perpendicular to the plane of

171   sedimentation with a rock saw, and the exposed internal surface was polished. The samples

172   were then mounted inside an EDAX Orbis Micro XRF Analyzer to construct elemental maps

173   at a spatial resolution of 30 μm (Rh tube at 30kV, 500 μA, no filter, 300 ms dwell time, 30

174   μm capillary beam). Selected zones were analyzed at higher resolution by electron

175   microprobe energy-dispersive spectroscopy (EDS) elemental mapping (JEOL JXA 8600

176   Superprobe with Noran Voyager automation, 15kV accelerating voltage, Si/Li detector, 1 μm

177   beam). General electron microprobe maps were produced at 4 μm spatial resolution, and

178   subsequent targeted (1 μm-resolution) maps were made of the regions around selected

179   particles. Additionally, microfossils located in the epoxy embedded samples and isolated from

180   dried sediment powders were analyzed by scanning electron microscopy (SEM), to produce

181   micrographs and SEM-EDS spot measurements of interior mineral concretions.

182

183   3.2 Porewater sampling and analysis

184   Multicores (~0-60 cm) and gravity cores (~0-4 m) were taken for porewater analysis.

185   Porewater was analyzed for methane (CH_4, one parallel core) and major element and nutrient

186   chemistry (a second parallel core). All cores were pre-drilled with 1.5 cm diameter holes at

187   regular depth spacing, and taped prior to coring. Upon recovery, cutoff syringes were inserted

188   through the holes to extract wet sediment samples.

189

190   For the CH_4 analyses, precisely 10 ml wet sediment was extracted from each hole and

191   transferred immediately to a 65 ml glass bottle filled with saturated sodium chloride (NaCl)

192   solution. This bottle was then closed with a rubber stopper and screwcap, and a headspace of

193   10 ml N_2 gas was inserted. Methane concentrations in the headspace of the 65 ml glass bottles

194   were determined by injection of a subsample into a Thermo Finnigan Trace GC gas

195   chromatograph (flame ionization detector, Restek Q-PLOT column of 30m length, 0.32mm

196   internal diameter, oven temperature 25 °C). Data were then back-calculated to the original

197   porewater concentrations (porosity was calculated from water content data in the multicore

198   samples and assumed constant in the gravity core).

199

200   For the major element and nutrient analysis, approximately 20 ml wet sediment was

201   extracted from each hole. The cutoff syringe was capped with parafilm and transferred to a

202   nitrogen-filled glovebox, where the contents were transferred to a centrifuge tube. Samples

203   were centrifuged at 2500 g for 10-30 min and transferred back to the glovebox. Supernatant

204   porewaters were then filtered through 0.45 μm disposable filters and collected for

205   subsampling.

206

207   One supernatant porewater subsample was taken for analysis of hydrogen sulfide

208   (based on pH measurements at the depth of porewater sulfide maxima, assumed to be present

209   as HS^-). A 0.5 ml subsample was immediately transferred to 2 ml of 2% zinc (Zn)-acetate

210   solution after return to the glovebox, to precipitate zinc sulfide (ZnS), and stored at 5 °C.

211   Hydrogen sulfide concentrations were estimated spectrophotometrically by complexation of

212   the ZnS precipitate in an acidified solution of phenylenediamine and ferric chloride

213   (Strickland and Parsons, 1972).

214

215   A second supernatant porewater subsample was taken for analysis of P, Fe, Mn, Ca

216   and sulfur (S) by ICP-OES (acidified to 1M HCl, stored at 5 °C). Hydrogen sulfide was

217   assumed to be released during the initial acidification, thus S data is assumed to represent

218   sulfate (SO_4^{2-}) only. Comparison between ICP-OES-derived P and autoanalyzer-derived

219   HPO_4^{2-} concentrations suggest a contribution from dissolved organic phosphorus (DOP) at all

220   sites of < 20 μmol/L (not shown). Hence, ICP-OES-derived P is assumed approximately equal

221   to phosphate. ICP-OES-derived Fe, Mn and Ca data are assumed to represent Fe^{2+}, Mn^{2+} and

222   Ca^{2+}, respectively.

223

224   A third supernatant porewater subsample was taken for analysis of ammonium (NH_4^+)

225   and stored at -20 °C. Ammonium was determined spectrophotometrically on an autoanalyzer

226   using the phenol hypochlorite method (Riley, 1953). A fourth subsample was titrated for total

227   alkalinity with 0.01M HCl.

228

229   3.3 Bulk sediment sampling and analysis

230   Multicores from all sites were sliced onboard in a N_2-filled glovebox immediately

231   after recovery. To obtain gravity core sediment samples from site F80, sediment residue was

232   taken from the centrifuge tubes used for porewater extraction. Gravity core sediment samples

233   from site LL19 were taken from a separate core sliced in a glovebox (Table 1). Sediment

234   samples from all cores were stored at -20°C before being freeze-dried (including an estimate

235   of water content for non-centrifuged samples), powdered and ground in an agate mortar inside

236   an argon-filled glovebox.

237

238   From each sediment sample, aliquots of 0.5 g dried sediment were decalcified by

239   shaking in excess 1M HCl, initially for 12 h and for a further 4 h after addition of new acid.

240   Tests have shown that the amount of organic carbon hydrolyzed by this protocol is negligible

241   (van Santvoort et al., 2002). The decalcified sediment was dried, ground in an agate mortar

242   and analyzed by combustion for organic carbon (C_{org}) using a Fisons NA 1500 NCS

243   (precision and accuracy <2% based on an atropine/acetanilide standard calibration and

244   checked against internal laboratory standard sediments).

245

246   A second 0.1 g aliquot of dried sediment was dissolved in 2.5 ml HF (40 %) and 2.5

247   ml of a $HClO_4/HNO_3$ mixture, in a closed Teflon bomb at 90 °C for 12 h. The acids were then

248   evaporated at 190 °C and the resulting gel was dissolved in 1M HNO_3, which was analyzed

249   for P, Fe and Mn concentrations by ICP-OES (precision and accuracy <5 %, based on

250   calibration to standard solutions and checked against internal laboratory standard sediments).

251

252   A third 0.1 g aliquot of dried sediment was subjected to the SEDEX sequential

253   extraction procedure to determine the solid-phase partitioning of phosphorus (Ruttenberg,

254   1992). All water (H_2O) rinses were omitted from the original protocol (see Slomp et al.,

255   1996), but three magnesium chloride ($MgCl_2$) rinses were included. The full speciation is

256   shown in Table 2 with the expected P phases extracted in each step indicated. The initial 1M

257    $MgCl_2$ and citrate- dithionite- bicarbonate (CDB) rinses were performed inside the glovebox,

258   to eliminate the potential conversion of CFA to Fe-oxyhydroxide- bound P due to pyrite

259   oxidation upon oxygen exposure (Kraal et al., 2009). Phosphate in all rinses was analyzed

260   colorimetrically by the ammonium heptamolybdate - ascorbic acid method (precision and

261   accuracy <2 %, based on calibration to standard solutions and checked against internal

262   laboratory standard sediments), with the exception of the CDB rinse, in which P was analyzed

263   by ICP-OES.

264

265   **4. RESULTS**

266

267   4.1 Microanalysis

268   The electron microscope-EDS maps of the shallow sediments from site F80 show a

269   heterogeneous P distribution (Fig. 2a). At the 4 μm resolution of the general map, most P

270   enrichments are visible as single pixels or small clusters of pixels (Fig. 2a, b). Many of the

271   brightest pixels in the P maps are also bright in the corresponding maps of Fe (Fig. 2b),

272   indicating the presence of Fe-phosphates in these sediments. A 1 μm-resolution map centered

273   on one such enrichment (Fig. 2c) suggests 2D particle dimensions in the range of ~10 μm,

274   although the morphology of the particles remains difficult to resolve. Some of the Fe-P

275   enrichments also coincide with S (box 1 in Fig. 2a). Similar Fe-P enrichments are present

276   throughout the deeper sections of the sediments at F80, but are only infrequently observed at

277   LL19.

278

279   At specific depths at both F80 and LL19, layers of globular 100-500 μm-scale

280   enrichments of P coincide with Ca and Mn. These enrichments are large enough to be

281   resolved at the 30 μm resolution of the Micro XRF maps (Fig. 3), and indicate P associated

282   with Mn-Ca-carbonates (hereafter *Ca-rhodochrosites*). Similarly to the Fe-P enrichments,

283   these Ca-Mn-P enrichments are substantially more concentrated in the sediments at F80 than

284   in those at LL19.

285

286   Many circular 50-200 μm-scale enrichments of Ca and P are present in the Micro XRF

287   maps at all depths at both F80 and LL19, associated with microfossils in the sediments (Fig.

288   4a). The largest observed enrichments are related to unidentified spherical palynomorphs of

289   up to 200 μm in diameter (Fig. 4b). SEM-EDS analysis of these specimens reveals

290   concretions within the palynomorphs which are rich in Ca, P and oxygen (O), suggesting a

291   form of apatite (Fig. 4b).

292

293   4.2 Porewater analysis

294   At site F80, a pronounced SMT is present in the upper 70 cm of the sediments, as

295   indicated by the opposing gradients of SO_4^{2-} and CH_4 and a strong maximum in HS^- at 24 cm

296   depth (Fig. 5a). The addition of HCO_3^- and HS^- to the porewaters at this depth also generates a

297   small peak in the alkalinity profile, which otherwise shows the convex asymptotic increase

298   with depth typical of anaerobic, organic rich sediments. At site LL19, the SMT is not present

299   in the depth interval sampled. Sulfate concentrations decline with increasing depth but are not

300   fully exhausted within the analyzed 5 m, while CH_4 concentrations are negligible throughout

301   the core and no distinct peak is observed in HS^- (Fig. 5b).

302

303   Porewater trends for most other components are similar between sites F80 and LL19.

304   Ammonium concentrations display a convex asymptotic increase with depth. Phosphorus and

305   Mn^{2+} concentrations increase with depth until 70 cm but decline thereafter. Iron (Fe^{2+})

306   displays low but stable values at all depths, while Ca^{2+} increases slightly with depth (Fig. 5a,

307   b). Maximum NH_4^+, P and Mn^{2+} values are all higher at F80 than at LL19.

308

309   4.3 Multicore P speciation

310   The SEDEX extraction scheme was applied to multicore sediments from both deep-

311   basin sites (F80 and LL19) and from the shallow reference site LF1. The P distributions at

312   each of the three sites differ markedly from one another. Site F80 shows the highest total P

313   concentrations, principally contributed by Org-P and CDB-P (Fig. 6a). Notably at this site,

314   CDB-P shows a slight decline from the sediment surface downwards but never falls below 10

315   µmol/g after ~5 cm depth. Site LL19 shows intermediate total P concentrations, with

316   enrichments of Org-P and CDB-P present in the upper 10 cm of the sediments (Fig. 6b). LF1

317   shows the lowest total P concentrations, but a clear exponential decay in CDB-P from high

318   surface values to a background of 3-4 µmol/g (Fig. 6c). Acetate-P concentrations are

319   generally constant with depth at all sites. The only exception is a single large peak in Acetate-

320   P at 29 cm depth at site F80 (Fig. 6a).

321

322   4.4 Gravity core P speciation and bulk sediment chemistry

323   The depth intervals corresponding to known periods of enhanced Baltic-wide anoxia

324   during the Littorina Sea stage are indicated by C_{org} enrichments in the sediments of F80 and

325   LL19 (Fig. 7). Due to the shorter absolute core length and higher sedimentation rate at F80,

326   the Early Holocene anoxic interval is not captured at this site.

327

328   Throughout the gravity core records, total P concentrations are higher at F80 than at

329   LL19, due to higher concentrations of Org-P, CDB-P and, intermittently, Acetate-P (Fig. 7).

330   The maximum Org-P enrichments at both sites occur during intervals of enhanced Baltic-wide

331   anoxia. However, while small CDB-P and Acetate-P maxima also occur during Baltic-wide

332   anoxic intervals at LL19, far stronger CDB-P and Acetate-P maxima occur during the

333   intervening oxic periods at F80 (Fig. 7).

334

335   Concentrations of Ca and Mn are substantially higher at F80 than at LL19, indicating

336   higher concentrations of Mn-Ca-carbonates in the sediments at the former site (Fig. 7).

337   Furthermore, Ca and Mn concentrations increase with depth at F80, with occasional maxima

338   superimposed onto this trend. Both the trend and occasional maxima coincide with those

339   observed in the profile of Acetate-P.

340

341   **5. DISCUSSION**

342

343   Our results suggest that three principal P-bearing authigenic mineral phases are

344   present in the sediments of the deep basins of the Baltic. The following sections will discuss

345   the formation mechanisms of each phase in turn, before addressing the spatial and temporal

346   context of P-bearing mineral authigenesis in the Baltic, and the broader implications for

347   understanding the controls on P burial in marine sediments.

348

349   5.1 Fe (II) phosphate authigenesis

350   The CDB buffer solution of the SEDEX procedure is expected to dissolve both Fe-

351   oxyhydroxide associated P (Ruttenberg 1992) and Fe (II) phosphates such as vivianite

352   (Nembrini et al., 1983). Due to our strict anoxic procedures, contamination of the CDB-P

353   signal by neoformation of Fe-oxyhydroxide associated P during sample handling can be ruled

354   out (see Kraal et al., 2009). Furthermore, oxidation of primary Fe (II) phosphates to Fe (III)

355   phases such as kertschenite, koninckite and santabarbaraite (e.g. März et al., 2008) should

356   also have been avoided by our procedures. At site F80, CDB-P shows a slight decline from

357   the sediment surface downwards but never falls below 10 μmol/g after ~5 cm depth (Fig. 6,

358   7). This pattern suggests the presence of Fe oxyhydroxide-associated P in the surface

359   sediments, of which a portion undergoes dissolution, while the remainder is converted to Fe

360   (II) phosphates and buried (Fig. 6). The alternative hypothesis, namely deep preservation of

361   Fe oxyhydroxide-associated P, appears unlikely in the strongly euxinic sediments of F80, due

362   to the high reactivity of most ferric Fe minerals in the presence of hydrogen sulfide (Raiswell

363   and Canfield, 2012).

364

365   Our microanalysis results support the interpretation of Fe (II) phosphate authigenesis

366   in the modern sediments at F80. The electron microprobe EDS maps show 10-μm-scale

367   enrichments of Fe and P at 5 cm depth (Fig. 2). We counted 10 discrete Fe-P enrichments in

368   the 1 mm^2 map of Fig. 2a. The mean molar Fe/P of these enrichments, estimated from count

369   ratios in their EDS spectra, is 1.65. Although the microprobe-EDS approach may be regarded

370   as semi-quantitative only, this value appears significantly lower than those of Fe (III)

371   oxyhydroxide-phosphate complexes found in the redoxcline of the Baltic (Fe/P = 2.0-2.9,

372   Dellwig et al., 2010), and closer to that of Fe (II) phosphates such as vivianite,

373    $Fe_3(PO_4)_2 \cdot 8(H_2O)$, Fe/P = 1.5. We propose that the enrichments represent Fe (II) phosphate

374   minerals precipitated *in situ* in the sediments and therefore constitute a permanent P burial

375   phase. A rough extrapolation from the observed frequency of enrichments, assuming spherical

376   10 μm-diameter particles of pure vivianite and accounting for porosity and sediment density,

377   yields an expected vivianite-P concentration of ~15 μmol/g at 5 cm depth. This value is

378   similar to the 10 μmol/g background CDB-P observed at this depth.

379

380   Several previous observations of marine vivianite formation have cited bulk porewater

381   vivianite saturation due to a buildup of dissolved Fe and P below the SMT (e.g. März et al.,

382   2008; Schulz et al., 1994). However, both our SEDEX and microanalysis results suggest Fe

383   (II) phosphate formation in the uppermost 10 cm of the sediment at F80, thus well within the

384   SMT at this location (Fig. 5a). Furthermore, the high sedimentation rate of the upper

385   sediments (~0.5 – 1.1 cm/yr, estimated from ^{210}Pb data, not shown) confirms that Fe (II)

386   phosphate authigenesis at this depth has occurred very recently, implying a presently-active

387   process. Porewater conditions at F80 remained stable over three sampling years from 2009 to

388   2011 (Fig. 5a) and have likely been similar throughout the deposition of the upper 10 cm of

389   sediment at this site. Assuming the measured bulk porewater conditions to be representative

390   of those at the time of Fe (II) phosphate authigenesis, we calculated the saturation state of the

391   porewater with respect to vivianite at 5 cm depth (using PHREEQC, and applying the

392   saturation product of Al Borno and Tomson (1994), data from Fig. 5, and measured pH,

393   temperature and salinity). The results suggest that the porewater is in fact undersaturated with

394   respect to vivianite at this depth, principally due to the lack of free Fe (II) in the porewater.

395   This implies that Fe (II) phosphate authigenesis is not controlled by the composition of the

396   bulk porewater, but rather is directly coupled to the reduction of Fe-oxyhydroxides and

397   release of associated P, potentially in protected microenvironments within the sediments.

398

399   Under the strongly euxinic conditions of F80, rapid reductive dissolution by HS^- (i.e.

400   sulfidization) is likely to dominate over dissimilatory reduction (coupled to organic matter

401   degradation) as the major pathway of Fe-oxyhydroxide reduction in the sediments. If

402   sulfidization occurs in microenvironments, the probability of subsequent Fe (II) phosphate

403   precipitation may be determined by the highly local availability of Fe, P and S. The

404   precipitation of pyrite (FeS_2) is favored over that of vivianite in sulfidic systems across a

405   range of Eh conditions and HPO_4^{2-} activities (Nriagu, 1972). Hence, in most cases of

406   microenvironment sulfidization, pyrite would be expected to form as the dominant authigenic

407   phase. However, under high enough localized HPO_4^{2-} concentrations, or after exhaustion of

408   the local S supply relative to that of Fe and P, the precipitation of Fe (II) phosphates such as

409   vivianite may be favored. Authigenesis of these minerals coupled to Fe-oxyhydroxide

410   sulfidization would explain the occasional co-occurrence of Fe, P and S enrichments in the

411   microprobe maps (e.g. box 1 in Fig. 2a). Intriguingly, Fe (II) phosphate accumulations were

412   recently observed within cells of Deltaproteobacteria, the dominant sulfate-reducers of many

413   SMT environments (Milucka et al., 2012). Further study is required to determine whether the

414   Fe (II) phosphate accumulations observed in our samples are related to these microbial

415   processes.

416

417   A strongly contrasting upper-sediment CDB-P profile is observed at the shallow

418   reference site LF1, where CDB-P decays exponentially from the surface to background values

419   of 3-4 μmol/g (Fig. 6). Here, dissolution apparently removes most Fe and P from the CDB-

420   soluble pool with increasing sediment depth, with negligible conversion to Fe (II) phosphate

421   phases. Dissimilatory reduction of Fe-oxyhydroxides coupled to organic matter degradation is

422   likely quantitatively more important than sulfidization in the low-sulfide sediments at LF1.

423   Indeed, the dominance of the former process was shown by a recent modeling study of a site

424   in the south-west Baltic which experiences similar redox conditions and organic matter fluxes

425   to those at LF1 (Reed et al., 2011). Hence, despite the plentiful supply of Fe-oxyhydroxides at

426   such sites, substantial Fe (II) phosphate authigenesis does not occur, implying that a high rate

427   of sulfidization is also a prerequisite for this process. The upper-sediment CDB-P profile of

428   LL19 appears somewhat intermediate to those of the other two sites (Fig. 6), with a low

429   background concentration from 10-50 cm depth, but a recent shift towards higher

430   concentrations which coincides with an increase in Org-P. This pattern suggests that Fe (II)

431   phosphate autogenesis has recently been initiated at LL19, in response to the onset of the

432   modern anoxic interval (see also Fig. 7).

433

434   Although vivianite is the principal Fe (II) phosphate mineral to have been reported in

435   marine sediments, it should be noted that the series $Fe^{2+}_3(PO_4)_2 \cdot (H_2O)_n$ has multiple stable

436   phases, such as ludlamite $Fe_3(PO_4)_2 \cdot 4(H_2O)$ and phosphoferrite $Fe_3(PO_4)_2 \cdot 3(H_2O)$ (Moore,

437   1971). A series of hydroxylated Fe (II) phosphates also exists, including tinticite

438    $Fe_3(PO_4)_2(OH)_3 \cdot 3(H_2O)$ and lipscombite $Fe_3(PO_4)_2(OH)_2$ (Nriagu and Dell, 1974). The

439   analytical approaches in the present study are unable to differentiate between these phases.

440

441   5.2 Ca-rhodochrosite-P authigenesis

442   Intermittent layers rich in 100-500 μm-scale globular Ca-Mn-P enrichments are

443   observed in the micro XRF maps of the sediments at site F80 (Fig. 3), and to a lesser extent at

444   site LL19. The gravity core data for F80 show that extreme maxima in solid-phase Mn ($\leq$

445   14%) and Ca ($\leq$ 3%) consistently coincide with maxima in Acetate-P (Fig. 7), confirming the

446   association of P with Ca-rhodochrosite at this site. Ca-rhodochrosite has been reported in

447   many previous studies of Baltic Sea sediments (e.g. Jakobsen and Postma, 1989; Manheim,

448 1982; Suess, 1979), and is believed to form when Mn oxide (MnO_x) packets emplaced at the

449 sediment-water interface during inflow events are converted to carbonates after the re-

450 establishment of anoxic, high-alkalinity conditions (Heiser et al., 2001; Huckriede and

451 Meischner, 1996; Sternbeck and Sohlenius, 1997). Prior to these inflow events, bottom waters

452 are rich in both dissolved Mn^{2+} (Neretin et al., 2003) and HPO_4^{2-} (Gustafsson and Stigebrandt,

453 2007). The association of P with particulate Mn thus most likely occurs during inflow events,

454 upon the initial massive precipitation of MnO_x. This is supported by recent observations of

455 particulate MnO_x–P in the vicinity of the modern redoxcline (Dellwig et al., 2010). During the

456 subsequent conversion of MnO_x to Ca-rhodochrosite, phosphate apparently substitutes for

457 carbonate in the rhodochrosite structure, generating mixed Mn-Ca-carbonate-phosphate

458 phases as reported by Suess (1979).

459

460   Background sedimentary concentrations of Mn and Ca also increase downcore at site

461 F80 (Fig. 7a), implying syn-sedimentary precipitation of Ca-rhodochrosite as suggested

462 previously for Baltic sediments by Carman and Rahm (1997) and Heiser et al. (2001).

463 Background Acetate-P shows a slight concomitant increase (Fig. 7a), and porewater

464 concentrations of both Mn and P decrease from ~50 cm to the base of the core (Fig. 5a).

465 These observations suggest that some P is also incorporated into the syn-sedimentary

466 precipitated rhodochrosite phase. We suspect that emplaced Ca-rhodochrosite layers undergo

467 stepwise recrystallization after burial, allowing Mn and P to accumulate in the upper

468 porewaters and be drawn down at greater depth. This implies that the Ca-rhodochrosites are

469 only metastable at the time of their initial crystallization, as previously noted by various

470 authors (e.g. Jakobsen and Postma 1989; Sternbeck and Sohlenius 1997) who showed that

471 typical Baltic rhodochrosite Mn/Ca ratios fall within the large solid-solution miscibility gap in

472 the system $CaCO_3$-$MnCO_3$-H_2O (Middelburg et al., 1987).

473

474   5.3 Apatite precipitation in microfossils

475   Our microanalysis results show the frequent presence of apatite concretions within

476   spherical palynomorphs and other microfossils at both F80 and LL19 (Fig. 4). The

477   concretions in the palynomorphs have a soft texture and can be easily cut with a knife,

478   suggesting a poorly crystalline material possibly aggregated with organic matter. The SEM-

479   EDS spectra of the concretions often show small peaks of fluorine (F) beside those of C and O

480   (Fig. 4b), suggesting the apatite phase present to be CFA. However, since the measured C and

481   O may derive from either carbonate in CFA, or from organic matter, deducing the precise

482   stoichiometry of the apatite phase is not possible from these results. Sodium (Na), Mn and

483   magnesium (Mg) are also detected in minor quantities, implying substitution of these

484   elements for Ca in the apatite structure. Extrapolations to estimate the contribution of these

485   concretions to total Acetate-P in the SEDEX extractions are sensitive to both the assumed

486   concentration of CFA within the poorly crystalline material, and the assumed CFA

487   stoichiometry. However, if CFA with the formula of $Ca_{10}(PO_4)_{4.6}(CO_3)_{1.32}F_{1.87}(OH)_{1.45}$

488   (Perrone et al., 2002) were to occupy 30% of the volume of all such palynomorphs in their

489   observed density in the sediments, this phase alone could account for the full ~10-15 μmol/g

490   background Acetate-P observed at both F80 and LL19 (Fig. 6, 7), implying a quantitatively

491   significant burial flux of P. Except for the effects of Ca-rhodochrosite-P precipitation and

492   recrystallization at F80 (described in Section 5.2), sedimentary Acetate-P remains roughly

493   constant with depth at both sites. This suggests that precipitation of CFA within biogenic

494   microenvironments occurs not in the sediments, as previously reported for conversion from

495   calcite (Manheim et al., 1975), but rather in the water column or at the sediment-water

496   interface. Furthermore, this burial flux of P has varied little throughout the Holocene.

497

498   Precipitation of CFA in seawater is inhibited by the presence of Mg^{2+} ions (Martens

499   and Harriss, 1970) and undersaturation with respect to precursor phases such as octacalcium

500   phosphate $Ca_4H(PO_4)_3 \cdot 2.5(H_2O)$, which may have higher saturation products than CFA itself

501   (Gunnars et al., 2004). Hence, the biogenic microenvironments in our samples must have

502   experienced significant localized enrichment of Ca^{2+} and/or HPO_4^{2-} to trigger the precipitation

503   of CFA. We speculate that degradation of organic material within confined

504   microenvironments may have led to enhanced localized HPO_4^{2-} concentrations and hence

505   supersaturation with respect to octacalcium phosphate. Notably, we did not observe P

506   enrichments within microenvironments associated with biogenic silica, suggesting that

507   diatom-related polyphosphate accumulations (Diaz et al., 2008) are of minor importance to P

508   burial in the Baltic. However, without suspended matter samples we cannot comment on the

509   possible role of polyphosphates as precursors to the apatite precipitation we observe, as

510   reported for the precipitation of hydroxyapatite in *Thiomargarita* bacteria (Schulz and Schulz,

511   2005). Interestingly, Acetate-P was not observed to be an important fraction of particulate P

512   in the water column of a silled fjord in another recent study (Diaz et al., 2012). This suggests

513   either that the apatite precipitation we observe takes place mainly at the sediment-water

514   interface, or that the palynomorphs and other microfossils in our samples – and hence the

515   available microenvironments for CFA precipitation – are specific to the Baltic.

516

517   5.4 Bathymetric controls on the distribution of authigenic P-bearing minerals

518   Both Fe (II) phosphates (indicated by CDB-P) and Ca-rhodochrosite-P (indicated by

519   peaks in Acetate-P) are more prevalent in the sediments at the deepest studied site, F80, than

520   at the slightly shallower LL19 (Fig. 6, 7). Due to its greater water depth (Table 1), F80

521   experiences the more severe and persistent bottom water euxinia of the two sites (Baltic

522   Environmental Database, http://nest.su.se/models/bed.htm). This spatial variability in redox

523   conditions ultimately controls the distribution of authigenic P-bearing minerals in the

524   sediments of the Baltic, with Fe (II) phosphates and Ca-rhodochrosite-P found primarily in

525   the deepest basins. Continuous shelf to basin 'shuttling' of the oxides of Fe and Mn has been

526   shown to focus these elements preferentially into the deepest parts of euxinic basins (Lyons

527   and Severman, 2006). In the Baltic, the spatial scale is apparently small enough, and the

528   downslope Fe-oxyhydroxide flux great enough, that deep basin sites such as F80 can

529   accumulate a surface-sediment pool of Fe-oxyhydroxides which have resisted dissolution in

530   the water column. This pool carries with it associated P, and under the euxinic conditions in

531   the deep basins, sulfidization triggers its partial conversion to Fe (II) phosphates (Section 5.1).

532   In contrast, MnO_x largely dissolves upon entering the euxinic basins, leading to accumulation

533   of Mn in the deep waters and intermittent massive reprecipitation of Mn oxides during inflow

534   events (Section 5.2).

535

536   The variable distribution of redox conditions in the Baltic during the Holocene has

537   also impacted the distribution of authigenic P-bearing minerals in the sediments on centennial

538   to millennial timescales. When comparing the gravity core records of F80 and LL19 (Fig. 7),

539   it can be seen that the maximum accumulation of CDB-P and Acetate-P at F80 occurred

540   during periods of oxic conditions throughout much of the Baltic. In contrast, slightly

541   enhanced CDB-P and Acetate-P burial at LL19 occurred during the Baltic-wide anoxic

542   intervals of the Early Holocene, MCA and late 20th century (the slight increase of CDB-P

543   burial at LL19 during the late 20th century is also visible in the upper 10 cm of the multicore

544   from this site, Fig. 6). The contrasting histories of authigenic P-bearing mineral accumulation

545   at the two sites can be explained in terms of the source area to basin sink area (S/B) concept

546   used by Raiswell and Anderson (2005) to explain variable rates of Fe enrichment in anoxic

547   basins. During generally oxic intervals of Baltic history, deep basin sites such as F80

548   apparently still experienced localized anoxia, due to their relatively restricted hydrography

549   and the oxygen demand of focused organic material. These 'pockets' of low-oxygen

550   conditions must have undergone massive focusing of Fe and Mn oxides - precursors to the

551   eventual authigenic P-bearing minerals - due to the large source area of the surrounding

552   sediments relative to the sink area of the basins themselves (i.e. high S/B conditions). In

553   contrast, during periods of expanded anoxia such as the MCA, the source area of Fe and Mn

554   oxides was relatively small, while the potential basin sink area was much greater (Fig. 8).

555   These 'low S/B' conditions led to a more homogeneous accumulation of authigenic P-bearing

556   minerals across a much wider area, including at site LL19.

557

558   5.5 Quantitative importance of authigenic P-bearing minerals to P burial in the Baltic

559   The complete suite of authigenic P-bearing minerals, including Fe (II) phosphates, Ca-

560   rhodochrosite-P and microfossil CFA, account for a substantial fraction of total P burial in the

561   deep basins of the Baltic. At F80, the authigenic contribution to total P during a typical 'oxic'

562   interval - such as the period between the MCA and modern anoxic intervals - is 50% (Table

563   3). The net Baltic-wide burial rate of authigenic P-bearing minerals during oxic intervals may

564   be roughly estimated by assuming that F80 is representative for all sediments below ~175 m

565   water depth, equivalent to a total sedimentary area of ~5000 km^2. A mean accumulation rate

566   of approximately 1760 tonnes P/yr into authigenic minerals is thus calculated for oxic

567   intervals (Table 3), while total P burial in the Baltic is estimated at around 14000 tonnes P/yr

568   (Bo Gustafsson, personal communication). This confirms that the authigenic component is a

569   quantitatively significant burial pathway for P during oxic intervals. Hence, the shuttling of Fe

570   and Mn oxide precursor phases into the deep basins may have helped to maintain generally

571   oxic conditions between the MCA and modern anoxic interval, by efficiently sequestering P

572   in a few euxinic deep basins.

573

574   During Baltic-wide anoxic intervals such as today, the spatial extent of authigenic P-

575 bearing mineral formation increases to include site LL19 and likely all sediments below the

576 redoxcline at ~100 m water depth (Fig. 8). However, the concentrations of Fe (II) phosphates

577 and Ca-rhodochrosite-P in the sediments at F80 are lower at such times because of the low

578 S/B conditions (Section 5.4). Due to the less focused occurrence of P-bearing mineral

579 authigenesis, and the higher rate of Org-P burial, we calculate an authigenic contribution of

580 just 21% to total P burial during the MCA at F80 (Table 3). Yet, if F80 is considered

581 representative for 60000 km^2 of sediments during anoxic intervals, the net burial rate of P into

582 authigenic minerals throughout the Baltic is 2540 tonnes P/yr (vs. 1760 tonnes P/yr in oxic

583 intervals). Due to the uncertainties involved, the most important conclusion of this exercise is

584 that the burial rate of authigenic P-bearing minerals is of a similar order of magnitude during

585 both oxic and anoxic intervals, but that its contribution to total P burial declines during anoxic

586 intervals due to enhanced burial of Org-P. Nevertheless, the significant burial of authigenic P-

587 bearing minerals we report during both oxic and anoxic intervals contrasts with a previous

588 study which suggested P burial in authigenic phases to be limited in the Baltic (Mort et al.,

589 2010). We suggest that the small number of true deep-basin sites investigated in that study

590 obscured the importance of authigenic phases to total P burial.

591

592 5.6 Wider implications for global sedimentary P burial

593   Major uncertainties still exist regarding the controls on P burial rates in marine

594 sediments, principally related to poor understanding of the processes which regulate the

595 sequestration of P into authigenic mineral phases. It is well established that low-oxygen

596 conditions increase the efficiency of P release during organic matter breakdown, as recorded

597 by higher sedimentary organic carbon to organic phosphorus ($C_{org}:P_{org}$) ratios under low-

598   oxygen conditions (Ingall et al., 1993; Jilbert et al., 2011; Slomp and Van Cappellen, 2007).

599   Furthermore, a similar negative correlation exists between bottom-water oxygen

600   concentrations and sedimentary organic carbon to total phosphorus ($C_{org}:P_{tot}$) ratios (Algeo

601   and Ingall, 2007), suggesting that P released from organic matter in low-oxygen environments

602   is not generally retained in the sediments. However, many of the datasets presented in the

603   compilation of Algeo and Ingall (2007) contain a large degree of scatter along the $C_{org}:P_{tot}$

604   axis, implying that P mineral authigenesis rates vary between environments of similar redox

605   conditions, exerting a secondary control on the total burial rate of P.

606

607   Authigenic apatite phases such as CFA are commonly found in ocean margin

608   sediments (Filippelli and Delaney 1996; Ruttenberg and Berner 1993; Slomp et al., 1996), and

609   in some environments may act as a precursor to phosphorite deposits (Föllmi, 1996). Apatite

610   formation has been suggested to be accelerated by sulfur bacteria such as *Thiomargarita* and

611   *Beggiatoa* (Schulz and Schulz, 2005; Goldhammer at al., 2010), but the global distribution of

612   these genera is not yet known. Potentially, sedimentary environments of similar redox

613   conditions but contrasting bacterial assemblages may thus record different rates of CFA

614   formation, accounting for some of the scatter in the global $C_{org}:P_{tot}$ data of Algeo and Ingall

615   (2007). Alternatively, the bacteria may be abundantly present but the environmental

616   conditions in the sediment may not support CFA formation. Our results for the Baltic show

617   that the rate of Fe (II) phosphate and Ca-rhodochrosite-P authigenesis varies spatially and

618   temporally in connection with the shuttling of precursor Fe and Mn oxide phases into euxinic

619   basins. Total P burial in euxinic basins may thus depend upon the magnitude and distribution

620   of these particle shuttles. Although the flux of Fe and Mn oxides from surrounding continents

621   is the primary driver of submarine particle shuttles, the spatial distribution of low-oxygen

622   conditions in such basins modifies their magnitude and trajectory, and hence the burial rate of

623   P. For example at our deepest studied site, F80, localized euxinic conditions generally favor

624   intense P mineral authigenesis, raising the rate of total P burial relative to that expected under

625   the euxinic bottom-water conditions. However, the rate of authigenesis also decreases

626   markedly at this site during intervals of more widespread anoxia, despite the constancy of

627   euxinia in the deep basins themselves. Hence, site-specific redox conditions alone cannot be

628   used to predict the total rate of P burial without an understanding of their wider spatial

629   context.

630

631   **6. CONCLUSIONS**

632   Iron (II) phosphate authigenesis occurs in the sediments of the deep euxinic basins of

633   the Baltic Sea. In contrast to previously reported occurrences of Fe (II) phosphates in marine

634   sediments, authigenesis of these minerals in the Baltic is not driven by bulk porewater

635   saturation below the SMT. Rather, authigenesis occurs within the SMT in the upper

636   sediments, most likely during the rapid reductive dissolution of Fe-oxyhydroxides and release

637   of associated P by reaction with hydrogen sulfide. Phosphorus is also incorporated into Mn-

638   Ca-carbonates, which form after inflow events into the deep euxinic basins have precipitated

639   massive deposits of Mn oxides in the surface sediments. Throughout the Holocene, the burial

640   rate of P burial in these two authigenic phases has been greatest in the deepest basins, where

641   euxinia has persisted even during intervals of generally oxic conditions elsewhere in the

642   Baltic. Such conditions favor intense shuttling of Fe and Mn oxide precursor phases into a

643   restricted depositional area. A third authigenic P-bearing mineral, CFA, precipitates within

644   biogenic microenvironments in the water column or at the sediment-water interface and

645   contributes a relatively constant burial flux of P throughout the Baltic and throughout the

646   Holocene. Our observations suggest that total P burial in euxinic basins may be strongly

647   influenced by the distribution of submarine particle shuttles, partly accounting for the

648 observed scatter in predicted relationships between P burial rate and bottom-water redox

649 conditions worldwide.

650

662

663

664

665

666

667

668

669

670

671

672

673

674

675

676

677

678

679

680

681

682

683

684

REFERENCES

685

686 Al Borno A. and Tomson A. B. (1994) The temperature dependence of the solubility product

687   constant of vivianite. *Geochim. Cosmochim. Acta* **58,** 5373-5378.

688 Algeo T. and Ingall E. D. (2007) Sedimentary C_{org}:P ratios, paleocean ventilation, and

689   Phanerozoic atmospheric pO_2. *Palaeo., Palaeo., Palaeo.* **256,** 130–155.

690 Burns S. J. (1997) Early diagenesis in Amazon fan sediments. In *Proceedings of the Ocean*

691   *Drilling Program, Scientific Results,* Vol. **155** (eds. R. D. Flood, D. J. W. Piper, A.

692   Klaus and L. C. Peterson).

693 Carman R. and Rahm L. (1997) Early diagenesis and chemical characteristics of interstitial

694   water and sediments in the deep deposition bottoms of the Baltic proper. *J. Sea Res.*

695   **37,** 25-47.

696 Conley D. J., Bjorck S., Bonsdorff E., Carstensen J., Destouni G., Gustafsson B. G., Hietanen

697   S., Kortekaas M., Kuosa H., Meier H. E. M., Muller-Karulis B., Nordberg K., Norkko

698   A., Nurnberg G., Pitkanen H., Rabalais N. N., Rosenberg R., Savchuk O. P., Slomp C.

699   P., Voss M., Wulff F. and Zillen L. (2009) Hypoxia-Related Processes in the Baltic

700   Sea. *Environ. Sci. Technol.* **43,** 3412-3420.

701 Dellwig O., Leipe T., März C., Glockzin M., Pollehne F., Schnetger B., Yakushev E. V.,

702   Boettcher M. E. and Brumsack H. (2010) A new particulate Mn-Fe-P-shuttle at the

703   redoxcline of anoxic basins. *Geochim. Cosmochim. Acta* **74,** 7100-7115.

704

705   Diaz J., Ingall E., Benitez-Nelson C., Paterson D., de Jonge M. D., McNulty I., and Brandes J.

706   A. (2008) Marine polyphosphate: a key player in geologic phosphorus sequestration.

707   *Science* **320,** 652-655.

708   Diaz J. M., Ingall E. D., Snow S. D., Benitez-Nelson C. R., Taillefert M., and Brandes J. A.

709   (2012) Potential role of inorganic polyphosphate in the cycling of phosphorus within

710   the hypoxic water column of Effingham Inlet, British Columbia. *Global Biogeochem.*

711   *Cy.* **26,** GB2040.

712   Diaz R. J. and Rosenberg R. (2008) Spreading dead zones and consequences for marine

713   ecosystems. *Science* **321,** 926-929.

714   Elmgren R. (2001) Understanding human impact on the Baltic ecosystem: Changing views in

715   recent decades. *Ambio* **30,** 222-231.

716   Filippelli G. and Delaney M. (1996) Phosphorus geochemistry of equatorial Pacific

717   sediments. *Geochim. Cosmochim. Acta* **60,** 1479-1495.

718   Föllmi K. B. (1996) The phosphorus cycle, phosphogenesis and marine phosphate-rich

719   deposits. *Earth, Sci. Rev.* **40,** 55-124.

720   Goldhammer T., Brüchert V., Ferdelman T. G., and Zabel M. (2010) Microbial sequestration

721   of phosphorus in anoxic upwelling sediments. *Nat. Geosci.* **3,** 557-561.

722   Gunnars A., Blomqvist S., and Martinsson C. (2004) Inorganic formation of apatite in

723   brackish seawater from the Baltic Sea: an experimental approach. *Mar. Chem.* **91,** 15-

724   26.

725   Gustafsson B. G. and Stigebrandt A. (2007) Dynamics of nutrients and oxygen/hydrogen

726   sulfide in the Baltic Sea deep water. *J. Geophys. Res.- Biogeo* **112,** G02023.

727   Heiser U., Neumann T., Scholten J. and Stuben D. (2001) Recycling of manganese from

728   anoxic sediments in stagnant basins by seawater inflow: a study of surface sediments

729   from the Gotland Basin, Baltic Sea. *Mar. Geol.* **177,** 151-166.

730   Huckriede H. and Meischner D. (1996) Origin and environment of manganese-rich sediments

731   within black-shale basins. *Geochim. Cosmochim. Acta* **60,** 1399-1413.

732   Ingall E. D., Bustin R. M. and Van Cappellen P. (1993) Influence of water column anoxia on

733   the burial and preservation of carbon and phosphorus in marine shales. *Geochim.*

734   *Cosmochim. Acta* **57,** 303-316.

735   Intergovernmental Oceanographic Commission, International Hydrographic Organization and

736   British Oceanographic Data Centre (2003) *Centenary Edition of the GEBCO Digital*

737   *Atlas, published on CD-ROM on behalf of the Intergovernmental Oceanographic*

738   *Commission and the International Hydrographic Organization as part of the General*

739   *Bathymetric Chart of the Oceans*. British Oceanographic Data Centre, Liverpool, U.K.

740   Jahnke R., Emerson S., Roe K. and Burnett W. (1983) The present-day formation of apatite in

741   Mexican continental-margin sediments. *Geochim. Cosmochim. Acta* **47,** 259-266.

742   Jakobsen R. and Postma D. (1989) Formation and solid-solution behavior of Ca-

743   rhodochrosites in marine muds of the Baltic Deeps. *Geochim. Cosmochim. Acta* **53,**

744   2639-2648.

745   Jilbert T., de Lange G. and Reichart G. J. (2008) Fluid displacive resin embedding of

746   laminated sediments: preserving trace metals for high-resolution paleoclimate

747   investigations. *Limnol. Oceanogr.- Meth.* **6,** 16-22.

748   Jilbert T., Slomp C. P., Gustafsson B. G. and Boer W. (2011) Beyond the Fe-P-redox

749   connection: preferential regeneration of phosphorus from organic matter as a key

750   control on Baltic Sea nutrient cycles. *Biogeosciences* **8,** 1699-1720.

751   Kraal P., Slomp C. P., Forster A., Kuypers M. M. M. and Sluijs A. (2009) Pyrite oxidation

752   during sample storage determines phosphorus fractionation in carbonate-poor anoxic

753   sediments. *Geochim. Cosmochim. Acta* **73,** 3277-3290.

754   Lyons T. W. and Severmann S. (2006) A critical look at iron paleoredox proxies: new

755   insights from modern euxinic marine basins. *Geochim. Cosmochim. Acta* **70,** 5698-

756   5722.

757   März C., Hoffmann J., Bleil U., de Lange G. J. and Kasten S. (2008) Diagenetic changes of

758   magnetic and geochemical signals by anaerobic methane oxidation in sediments of the

759   Zambezi deep-sea fan (SW Indian Ocean). *Mar. Geol.* **255,** 118-130.

760   Manheim F., Rowe G. and Jipa D. (1975) Marine phosphorite formation off Peru. *J.*

761   *Sediment. Petrol.* **45,** 243-251.

762   Manheim F. T. (1982) Geochemistry of manganese carbonates in the Baltic Sea, *Stockholm*

763   *Contrib. Geol.* **37,** 145-159.

764   Martens C. S., and Harriss R. C. (1970) Inhibition of apatite precipitation in marine

765   environment by magnesium ions. *Geochim. Cosmochim. Acta* **34,** 621–625.

766   Middelburg J., de Lange G. J. and van der Weijden C. (1987) Manganese Solubility Control

767   in Marine Pore Waters. *Geochim. Cosmochim. Acta* **51,** 759-763.

768   Milucka J., Ferdelman T. G., Polerecky L., Franzke D., Wegener G., Schmid M., Lieberwirth

769   I.,Wagner M., Widdel F., and Kuypers M. M. M. (2012) Zero-valent sulphur is a key

770   intermediate in marine methane oxidation. *Nature* **491,** 541–546.

771   Moore P. B. (1971) The $Fe^{2+}_3 (H_2O)_n (PO_4)_2$ homologous series: Crystal-chemical

772   relationships and oxidized equivalents. *Amer. Mineral.* **56,** 1-17.

773   Mort H. P., Slomp C. P., Gustafsson B. G. and Andersen T. J. (2010) Phosphorus recycling

774   and burial in Baltic Sea sediments with contrasting redox conditions. *Geochim.*

775   *Cosmochim. Acta* **74,** 1350-1362.

776   Mortimer C. H. (1941) The exchange of dissolved substances between mud and water in

777   lakes. *J. Ecol.* **29**, 280-329.

778   Nembrini G., Capobianco J., Viel M. and Willams A. (1983) A Mossbauer and chemical

779   study of the formation of vivianite in sediments of Lago Maggiore (Italy). *Geochim.*

780   *Cosmochim. Acta* **47,** 1459-1464.

781   Neretin L. N., Pohl C., Jost G., Leipe T. and Pollehne F. (2003) Manganese cycling in the

782   Gotland Deep, Baltic Sea. *Mar. Chem.* **82,** 125-143.

783   Nriagu J. O. (1972) Solubility of vivianite and ion pair formation in the system $Fe_3(PO_4)_2$ -

784   H_3PO_4 - H_2O. *Geochim. Cosmochim. Acta*, **36,** 459-470.

785   Nriagu J. O, and Dell C. I. (1974) Diagenetic formation of iron phosphates in recent lake

786   sediments. *Amer. Mineral.* **59,** 934-946.

787 Perrone J., Fourest B., and Giffaut E. (2002) Surface characterization of synthetic and mineral

788   carbonate fluoroapatites. *J. Colloid Interface Sci.* **249,** 441– 452.

789 Raiswell R. and Anderson T. (2005) Reactive iron enrichment in sediments deposited

790   beneath euxinic bottom waters: constraints on supply by shelf recycling. *Geol. Soc.*

791   *Spec. Publ.* **248,** 179-194.

792 Raiswell R. and Canfield D. E. (2012) The iron biogeochemical cycle past and present.

793   *Geochemical Perspectives* **1,** 1-220.

794 Reed D. C., Slomp C. P. and Gustafsson B. G. (2011) Sedimentary phosphorus dynamics and

795   the evolution of bottom-water hypoxia: A coupled benthic-pelagic model of a coastal

796   system. *Limnol. Oceanogr.* **56,** 1075-1092.

797 Riley J. (1953) The spectrophotometric determination of ammonia in natural waters with

798   particular reference to sea-water. *Anal. Chim. Acta* **9,** 575-589.

799 Ruttenberg K. C. (1992) Development of a sequential extraction method for different forms of

800   phosphorus in marine sediments. *Limnol. Oceanogr.* **37,** 1460-1482.

801 Ruttenberg K. C.(1993) Reassessment of the oceanic residence time of phosphorus. *Chem.*

802   *Geol.*, **107,** 405–409.

803 Ruttenberg K. C. (2003) The global phosphorus cycle. *Treatise on Geochemistry* **8,** 585-643.

804 Ruttenberg K. C. and Berner R. A. (1993) Authigenic apatite formation and burial in

805   sediments from non-upwelling, continental-margin environments. *Geochim.*

806   *Cosmochim. Acta* **57,** 991-1007.

807   Ruttenberg K. C., and Goñi M. A. (1997). Depth trends in phosphorus and C:N:P ratios of

808   organic matter in Amazon Fan sediments: indices of organic matter source and burial

809   history. In *Proceedings of the Ocean Drilling Program, Scientific Results,* Vol. **155**

810   (eds. R. D. Flood, D. J. W. Piper, A. Klaus and L. C. Peterson).

811   Schulz H. N. and Schulz H. D. (2005) Large sulfur bacteria and the formation of phosphorite.

812   *Science* **307,** 416-418.

813   Schulz H., Dahmke A., Schinzel U., Wallmann K. and Zabel M. (1994) Early Diagenetic

814   Processes, Fluxes, and Reaction-Rates in Sediments of the South-Atlantic Ridge.

815   *Geochim. Cosmochim. Acta* **58,** 2041-2060.

816   Slomp C. P., and Van Cappellen P. (2007) The global marine phosphorus cycle: sensitivity to

817   oceanic circulation. *Biogeosciences* **4,** 155-171.

818   Slomp C. P., Epping E. H. G., Helder W. and van Raaphorst W. (1996) A key role for iron-

819   bound phosphorus in authigenic apatite formation in North Atlantic continental

820   platform sediments. *J. Mar. Res.* **54,** 1179-1205.

821   Sohlenius G., Emeis K.-C., Andrén E., Andrén T., and Kohly A. (2001) Development of

822   anoxia during the Holocene fresh-brackish water transition in the Baltic Sea. *Mar.*

823   *Geol.* **177,** 221-242.

824   Sternbeck J. and Sohlenius G. (1997) Authigenic sulfide and carbonate mineral formation in

825   Holocene sediments of the Baltic Sea. *Chem. Geol.* **135,** 55-73.

826   Stramma L., Johnson G. C., Sprintall J. and Morholz V. (2008) Expanding oxygen-minimum

827   zones in the tropical oceans, *Science* **320**, 655-658.

828   Strickland J. D. and Parsons T. R. (1972) *A practical handbook of seawater analysis*. Bulletin

829   167, Fisheries Research Board of Canada, Ottawa, Canada.

830   Suess E. (1979) Mineral phases formed in anoxic sediments by microbial decomposition of

831   organic-matter. *Geochim. Cosmochim. Acta* **43,** 339-352.

832   Tsandev I. and Slomp C. P. (2009) Modeling phosphorus cycling and carbon burial during

833   Cretaceous Oceanic Anoxic Events. *Earth Planet. Sc. Lett.* **286,** 71-79.

834   Turner R., Rabalais N. and Justic D. (2006) Predicting summer hypoxia in the northern Gulf

835   of Mexico: Riverine N, P, and Si loading. *Mar. Pollut. Bull.* **52,** 139-148.

836   Tyrrell T. (1999) The relative influences of nitrogen and phosphorus on oceanic primary

837   production. *Nature* **400,** 525-531.

838   Van Cappellen P. and Berner R. A. (1989) Marine apatite precipitation. In *Water-Rock*

839   *interaction,* Proc. 6th Intern. Symp. (WRI-6) (ed. D. L. Miles). A. A. Balkema,

840   Rotterdam, The Netherlands, pp. 707-710.

841   Van Cappellen P. and Ingall E. D. (1996) Redox stabilization of the atmosphere and oceans

842   by phosphorus-limited marine productivity. *Science* **271,** 493-496.

843   van Santvoort P. J. M., de Lange G. J., Thomson J., Colley S., Meysman F. J. R. and Slomp

844   C. P. (2002) Oxidation and origin of organic matter in surficial Eastern Mediterranean

845   hemipelagic sediments. *Aquat. Geochem.* **8,** 153-175.

846   Winterhalter B., Flodén T., Ignatius H., Axberg S. and Niemistö L (1981) Geology of the

847   Baltic Sea. In *The Baltic Sea. Elsevier Oceanographic Series* **30**, pp. 1-121 (ed. Voipo,

848   A.).

849   Zillen L., Conley D. J., Andrén T., Andrén E. and Bjorck S. (2008) Past occurrences of

850   hypoxia in the Baltic Sea and the role of climate variability, environmental change and

851   human impact. *Earth-Sci. Rev.* **91,** 77-92.

852

853

854

855

856

857

858

859

860

861

862

863

864

865

866

867

868

869

870

871

872

873

874

875 **TABLES**

876

877 Table 1. Sampling sites in the Baltic Sea presented in this study.

Site name and classification	Cruise	Co-ordinates (deg.-dec.)	Water depth (m)	Multicore analyses	Gravity core analyses
F80 Permanently hypoxic/anoxic (Group 2*)	R/V Aranda May/June 2009	19.8968 E 58.0000 N	191	-Sediment	
	R/V Heincke June/July 2010	19.8899 E 57.9928 N	181	-Porewater	-Porewater -Sediment
	R/V Pelagia May 2011	19.8969 E 57.9997 N	194	-Epoxy embedding and microanalysis	
LL19 Permanently hypoxic/anoxic (Group 2*)	R/V Aranda May/June 2009	20.3108 E 58.8807 N	169	-Sediment	-Sediment -Epoxy embedding and microanalysis
	R/V Heincke June/July 2010	20.3112 E 58.8762 N	173	-Porewater	-Porewater
	R/V Pelagia May 2011	20.3122 E 58.8771 N	175	-Epoxy embedding and microanalysis	
LF1 Oxic/seasonally hypoxic (Group 1*)	R/V Aranda May/June 2009	21.2807 E 57.9825 N	67	-Sediment	

878　　　* Classifications from Mort et al. (2010) and Jilbert et al. (2011).

879

880

881

882

883

884

885

886

887

888

889

890

891　Table 2. Stages of the SEDEX sequential extraction procedure (Ruttenberg, 1992). Expected

892　extracted phosphorus phases are listed, with references indicated when these differ from

893　Ruttenberg (1992).

Stage and code	Extractant	pH	Rinsing time (h)	Expected P phases	Reference
1 Ex-P	1M $MgCl_2$	8	0.5	-Exchangeable, loosely sorbed P	
2 CDB-P	Citrate-dithionite-bicarbonate (CDB)	7.5	8	-Fe oxyhydroxide-bound P -Vivianite	a
3 (CDB-P)	1M $MgCl_2$	8	0.5	-Any P resorbed during stage 2	
4 Acetate-P	Na acetate buffer	4	6	-Carbonate fluorapatite (CFA) -Hydroxyapatite -Ca-rhodochrosite-P	b
5 (Acetate-P)	1M $MgCl_2$	8	0.5	-Any P resorbed during stage 4	
6 Detrital-P **7**	1M HCl (ashing at 550 °C for 2 h)	0	24	-Detrital apatite minerals	
8 Organic P	1M HCl	0	24	-Organic P	

894

895　[a] Nembrini et al., 1983

896　[b] Suess, 1979

897

898

899

900

901

902

903

904

905

906

907

908 Table 3. Estimated burial rates of authigenic P ([CDB-P + Acetate-P] – [0.5*surface sediment

909 Acetate-P]) during the Medieval Climate Anomaly (MCA) and the period between the MCA

910 and the modern anoxic interval. Estimates include Fe (II) phosphates, Ca-rhodochrosite-P and

911 microfossil CFA (subtraction of half the surface-sediment Acetate-P concentration is based on

912 an assumed 50% contribution of microfossil-CFA to total Acetate-P).

913

Time interval	Authigenic P burial rate at F80 (μmol/cm^2/yr)	Total P burial rate at F80 (μmol/cm^2/yr)	Contribution of authigenic P to total P at F80 (%)	Area of similar sedimentation (km^2)	Baltic-wide authigenic P burial rate (tonnes/yr)
End of MCA to onset of modern anoxic interval	1.14	2.27	50	5000	1760
MCA	0.14	0.65	21	60000	2540

914

915

916

917

918

919

920

921

922

923

924

925

926

927

928   **FIGURE CAPTIONS**

929

930   Figure 1. Map of the Baltic Proper, showing the principal sub-basins and the locations of the

931   sites presented in this study. Bathymetric and coastline data are presented in Miller cylindrical

932   projection, taken from the General Bathymetric Chart of the Oceans (GEBCO) Digital Atlas

933   (Intergovernmental Oceanographic Commission et al., 2003).

934

935   Figure 2. (a) General electron microprobe-EDS maps of Fe, S and P on the internal surface of

936   an epoxy-embedded sediment block from F80 (5 cm depth). The maps are presented in true

937   vertical orientation and comprise a matrix of individual data points at 4 μm resolution. (b)

938   Zooms of the numbered boxes indicated in the Fe and P maps in *a*. The arrows indicate

939   examples of coincident enrichments of Fe and P. (c) Targeted electron microprobe-EDS maps

940   (at 1 μm resolution) in the vicinity of one Fe-and P-enriched particle located in *a*. The particle

941   is indicated by the arrow. A spot-measurement electron microprobe-EDS spectrum on the

942   same particle is shown to the right. Color scaling in all microprobe-EDS maps is determined

943   by the count intensity range within the mapped area, and subsequent adjustment of brightness

944   and contrast to optimize the visualization of features.

945

946   Figure 3. Micro XRF maps of Ca, P and Mn on the internal surface of an epoxy resin-

947   embedded sediment block from F80 (50 cm depth). The maps are presented in true vertical

948   orientation and comprise a matrix of individual data points at 30 μm resolution. The

949   histograms below each map indicate the distribution of pixels (data points) over the full range

950   of measured count intensities. The vertical axes have been expanded and truncated to

951   highlight the long-tailed distribution of the histograms; in reality, the modal peak for each

952   element extends several orders of magnitude beyond the depicted range. For each element, the

953   majority of the pixels thus record relatively low count intensities, while the majority of the

954   count range is represented by single pixels within 'hotspots' of extreme enrichment. Color

955   scaling in the maps is determined by the count intensity range within the mapped area, and

956   subsequent adjustment of brightness and contrast to optimize the visualization of features.

957

958   Figure 4. (a). Micro XRF maps of Ca and P on the internal surface of an epoxy resin-

959   embedded sediment block from LL19 (325 cm depth). The maps are presented in true vertical

960   orientation and comprise a matrix of individual data points at 30 μm resolution. The

961   histograms below each map indicate the distribution of pixels (data points) over the full range

962   of measured count intensities. The vertical axes have been expanded and truncated to

963   highlight the long-tailed distribution of the histograms; in reality, the modal peak for both

964   elements extends several orders of magnitude beyond the depicted range. For both elements,

965   the majority of the pixels thus record relatively low count intensities, while the majority of the

966   count range is represented by single pixels within 'hotspots' of extreme enrichment. Color

967   scaling in the maps is determined by the count intensity range within the mapped area, and

968   subsequent adjustment of brightness and contrast to optimize the visualization of features.

969   (b). SEM micrographs of spherical palynomorphs in epoxy-embedded sediments from F80,

970   ~2.5cm depth (left) and isolated from dried sediment samples from LL19, ~300 cm depth

971   (right). A spot-measurement SEM-EDS spectrum perfomed on the material within the

972   palynomorph in the right-hand micrograph is shown below. The exact position of the

973   measurement is indicated by the asterisk.

974

975   Figure 5. Porewater data from sites F80 and LL19. Multicore sulfate profiles from three

976   consecutive years (left) are shown to illustrate the lack of spatial and termporal variability

977   between the slightly offset sampling locations of each year (see Table 1). In the complete

978   profiles (right), filled circles indicate multicore samples, open circles indicate gravity core

979   samples.

980

981   Figure 6. SEDEX phosphorus speciation results for multicore sediments from F80, LL19 and

982   LF1. The stacked lines represent the concentrations of P extracted in each step of the SEDEX

983   procedure, while the white-filled circles represent total P as determined by ICP-OES.

984

985   Figure 7. Complete solid-phase sediment profiles from F80 and LL19. In F80 data, filled

986   circles indicate multicore samples, open circles indicate gravity core samples. LL19 data are

987   higher resolution and presented in line form only. Grey bars indicate C_{org} excursions

988   associated with widespread anoxic conditions in the Baltic during the Early Holocene (EH),

989   Medieval Climate Anomaly (MCA), and modern (Mod.) intervals.

990

991   Figure 8. Proposed bathymetric contours corresponding to the redoxcline during generally

992   oxic intervals of the Holocene history of the Baltic (left, 175 m) and during intervals of

993   widespread anoxia such as the MCA and today (right, 100 m). Sediments shallower than the

994   redoxcline act as a source for Fe and Mn oxide particle shuttles, while sediments deeper than

995   the redoxcline act as a sink. The rate of particle shuttling to a given basin controls the

996   formation of authigenic P-bearing minerals (see Section 5.4). Note the higher source area to

997   basin sink area (S/B) ratio during generally oxic intervals.
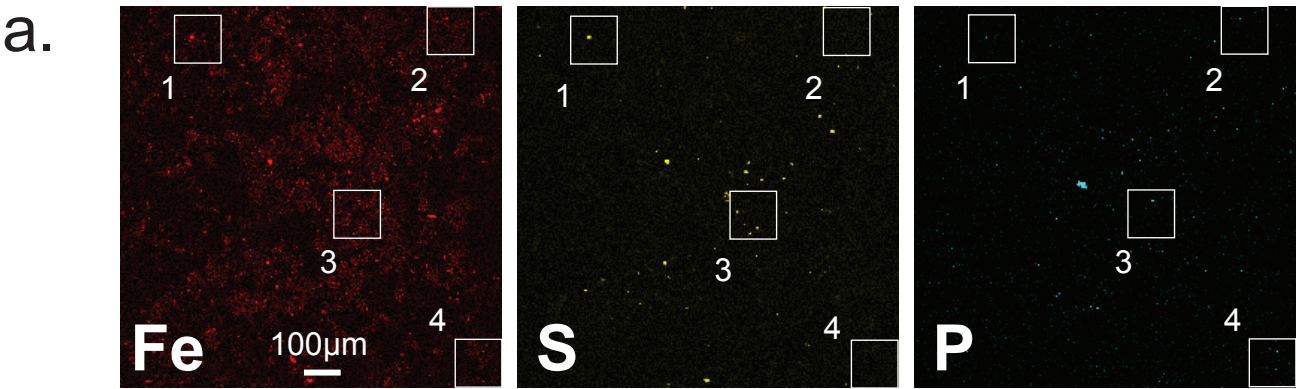
998

999

1000

1001

1002

1003

1004

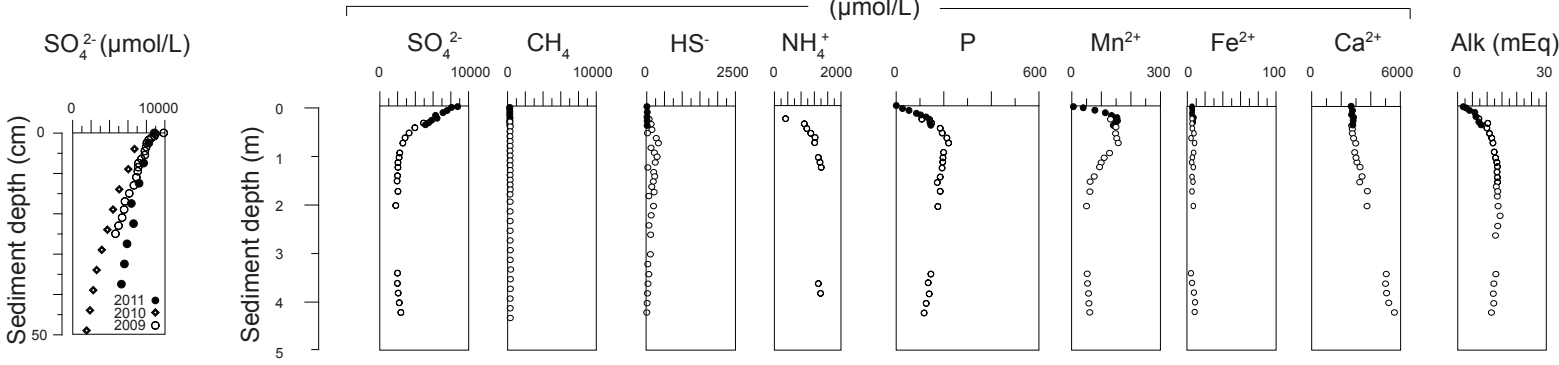Figure 1.pdf
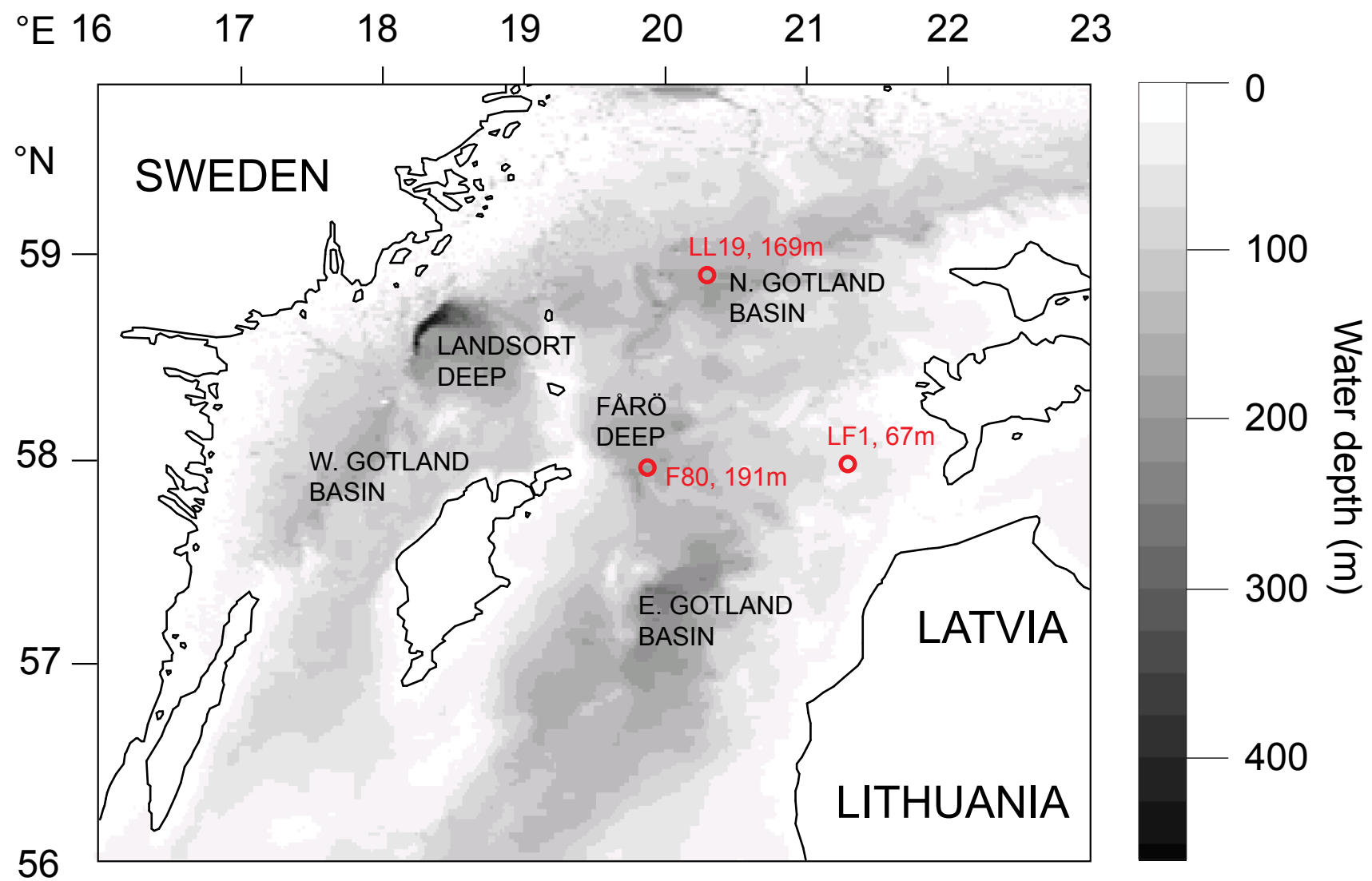
Figure 2.pdf
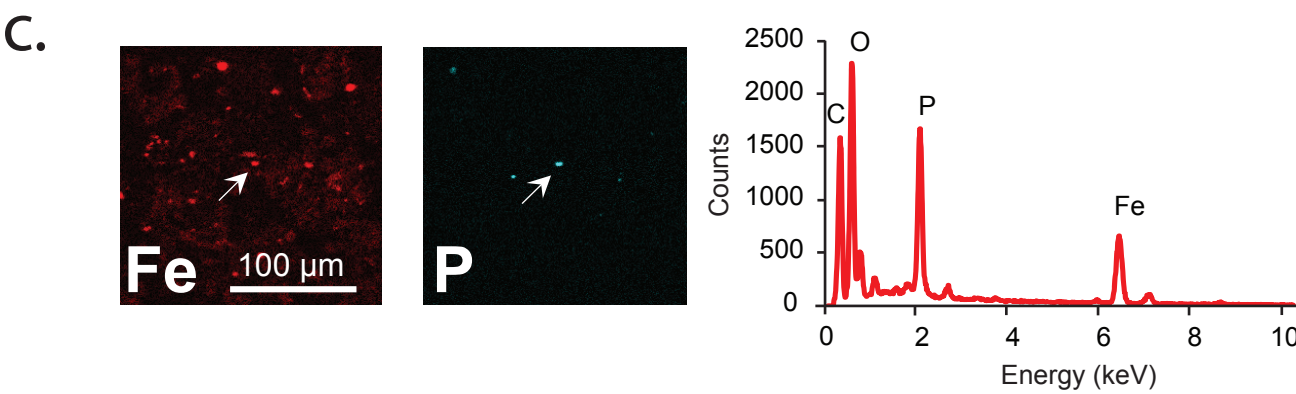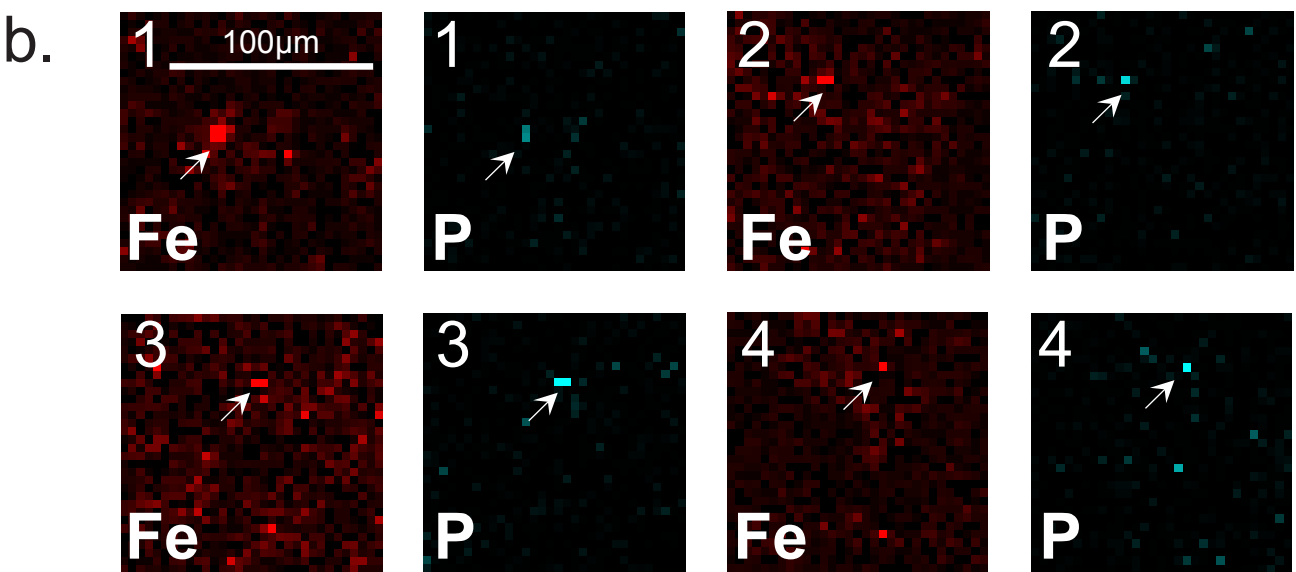
Figure 3.pdf
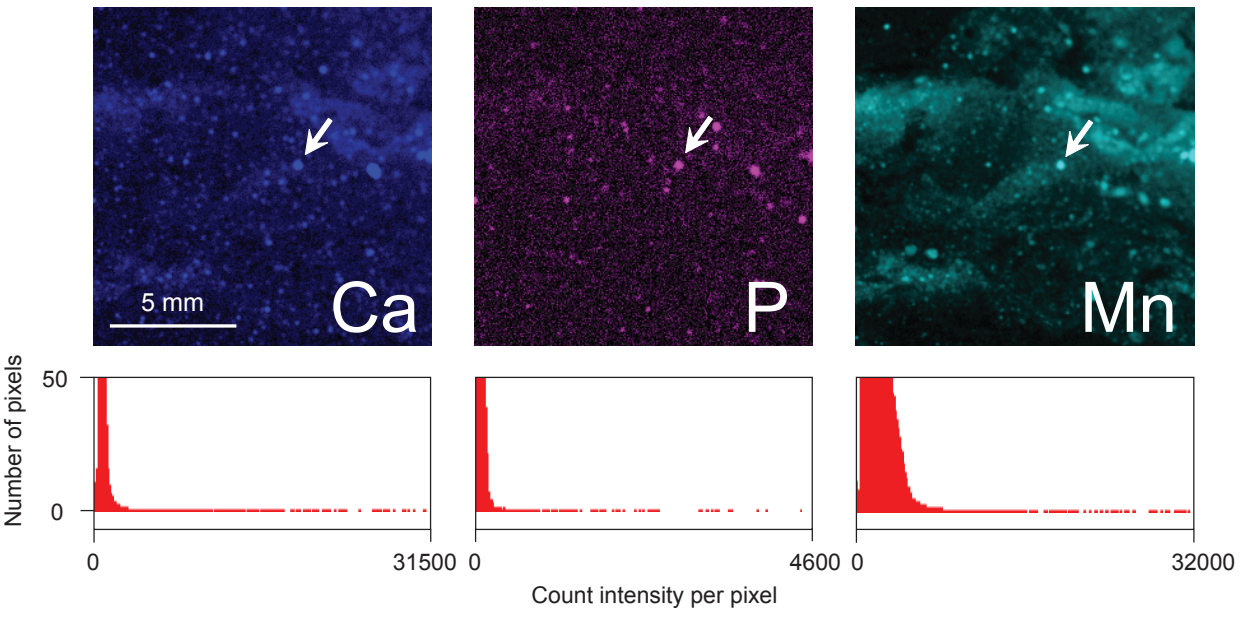
Figure 4.pdf

a.
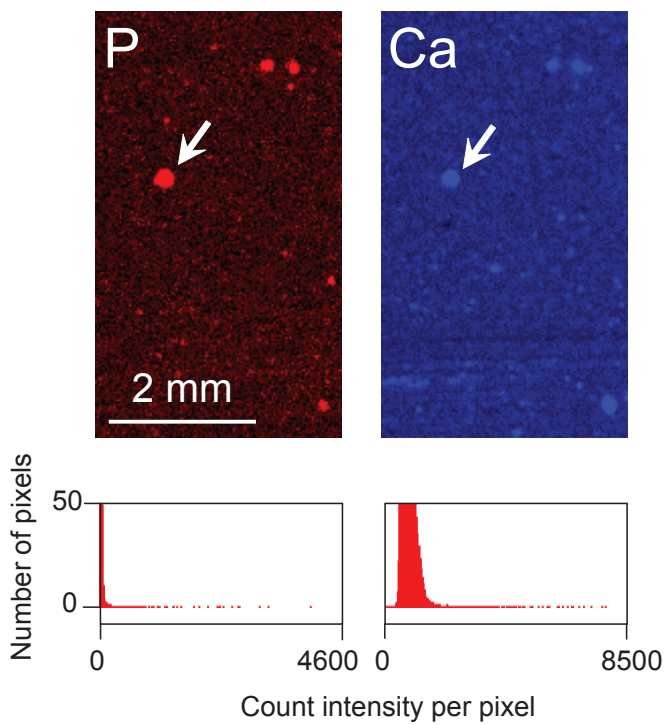
b.
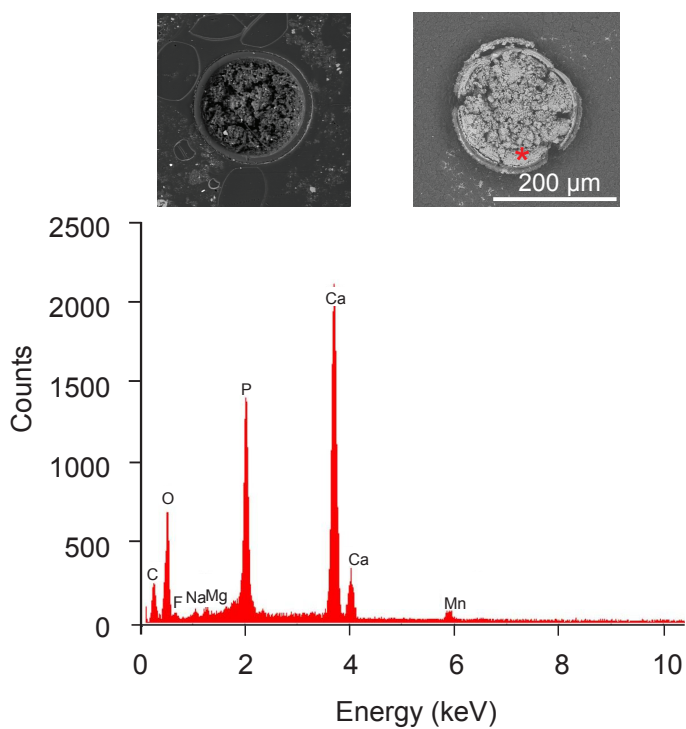
Figure 5.pdf

a. F80

b. LL19

Figure 6.pdf

a. F80
b. LL19
c. LF1

P (μmol/g)

Ex-P   CDB-P   Acetate-P   Detr-P   Org-P   ∘ P$_{tot}$ (ICP-OES)
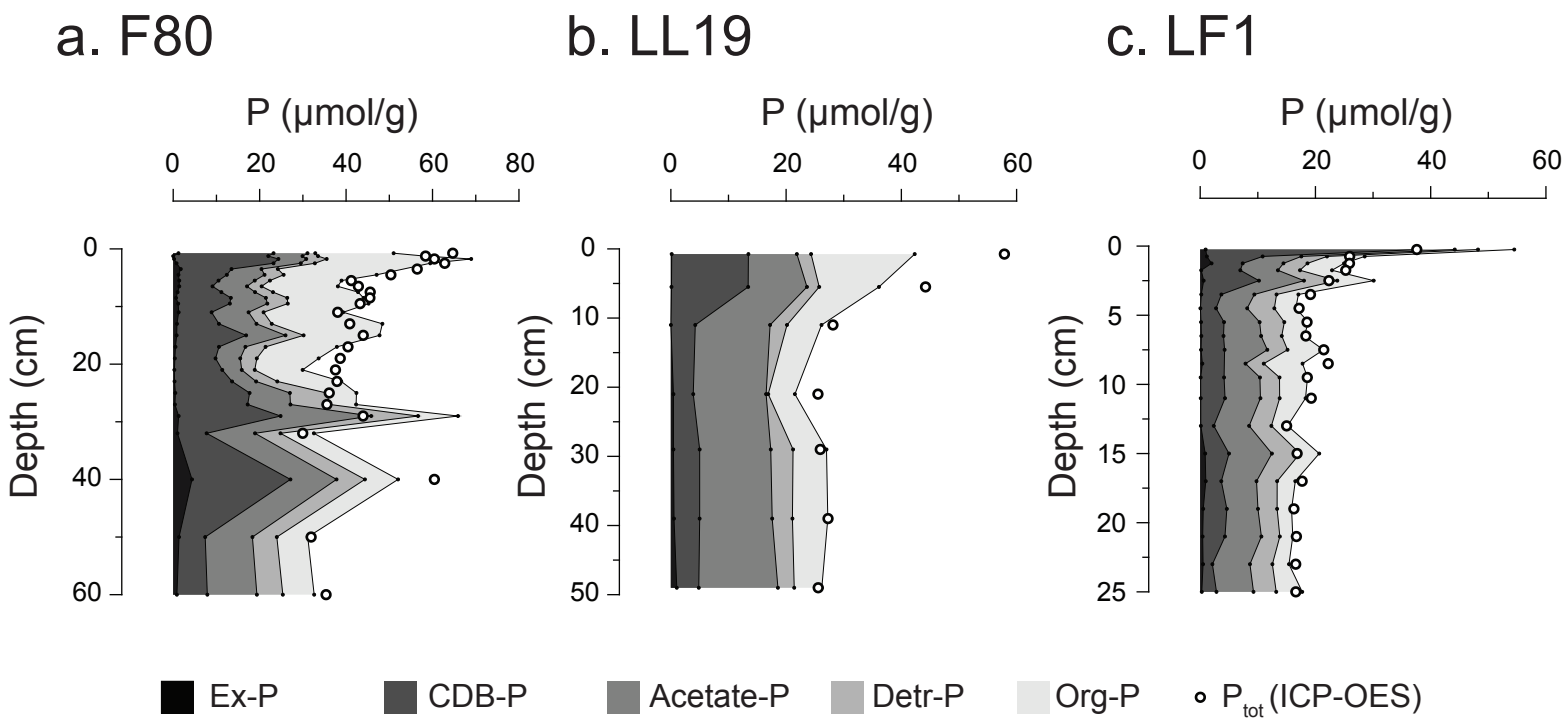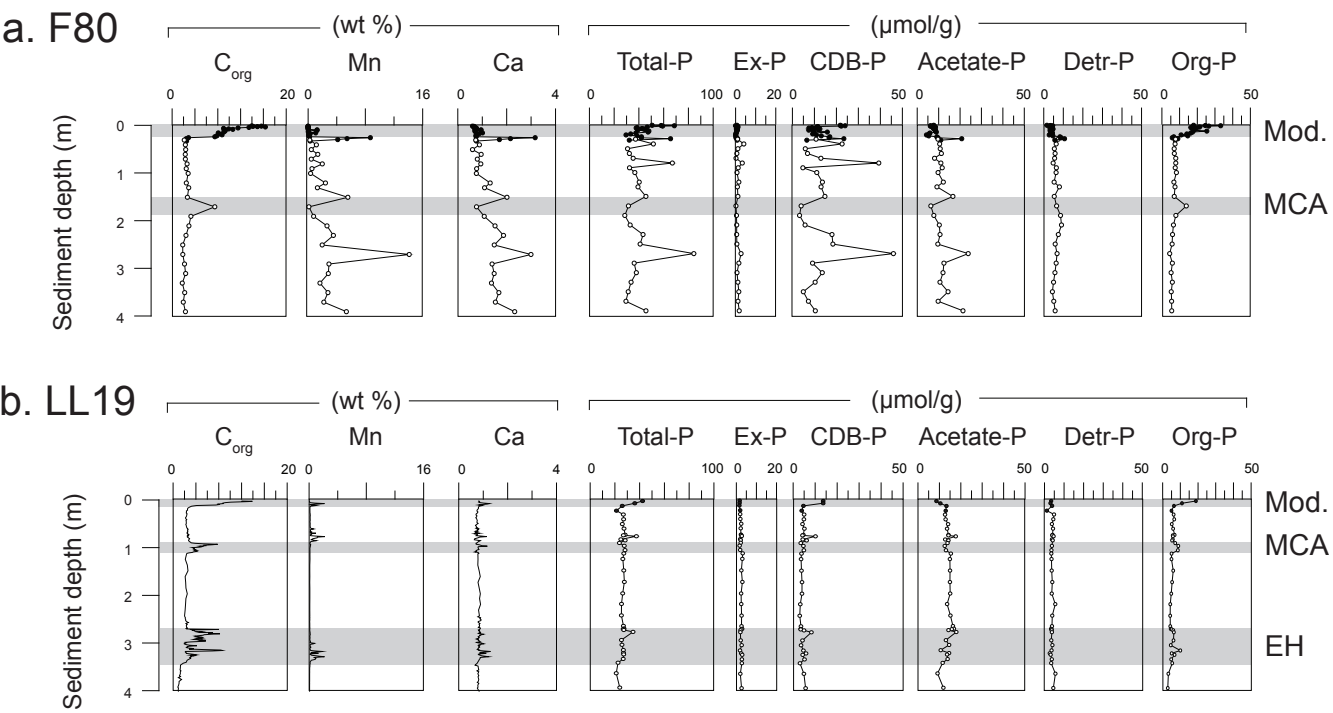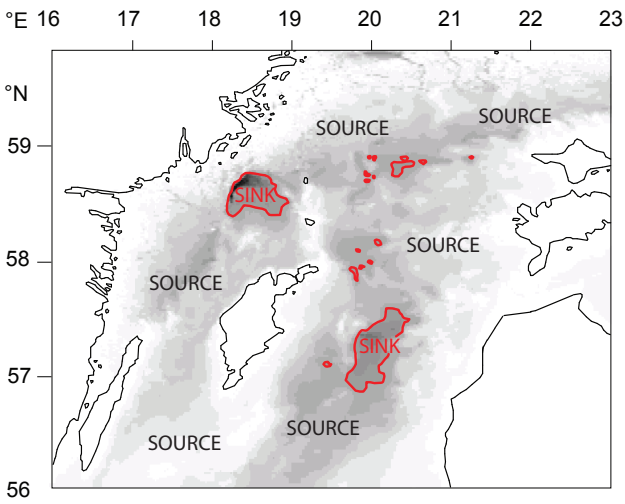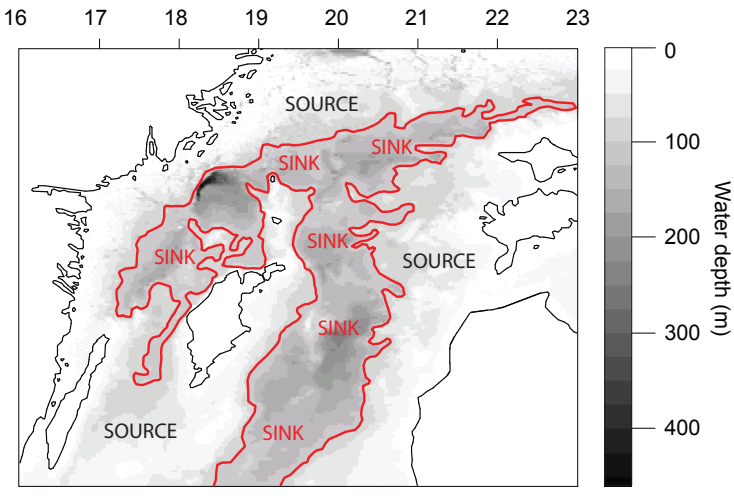
Figure 7.pdf

a. F80
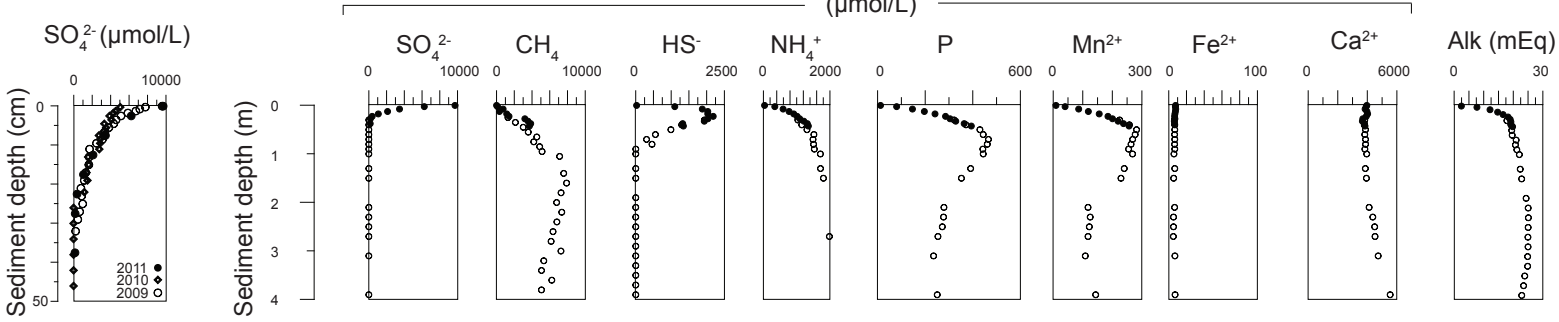
b. LL19

Figure 8.pdf

Oxic interval, 175 m

Anoxic interval, 100 m